Title

Stabilization of flavin mononucleotide by capturing its “tail” with porous organic polymers for long-term photocatalytic degradation of micropollutants

Authors

Tang, Peixin

Ji, Bolin

Sun, Gang

Publication Date

2022-08-01

DOI

10.1016/j.jhazmat.2022.128982

Peer reviewed

HHS Public Access

Author manuscript

J Hazard Mater. Author manuscript; available in PMC 2024 April 26.

Published in final edited form as:

J Hazard Mater. 2022 August 05; 435: 128982. doi:10.1016/j.jhazmat.2022.128982.

Stabilization of Flavin Mononucleotide by Capturing Its "Tail" with Porous Organic Polymers for Long-Term Photocatalytic Degradation of Micropollutants

Peixin Tang[a], **Bolin Ji**[b], **Gang Sun**[a,*]

[a]Department of Biological and Agricultural Engineering, University of California Davis, CA 95616, USA

[b]College of Chemistry, Chemical Engineering and Biotechnology, Donghua University, Shanghai, 201620, China

Abstract

Flavin mononucleotide (FMN) produces photo-induced reactive oxygen species (ROS), making it a bio-based and sustainable photosensitizer for micropollutant degradation. However, the rapid self-degradation of FMN under light poses challenges in practical applications. We propose for the first time to use porous organic polymer (POP) structures as particles and *in situ* grown on nanofibrous membranes to capture the ribityl side chain ("tail") of FMN by electrostatic-driven guest-host interaction. By restraining the free bending mode of FMN in POP, its self-degradation is highly inhibited, showing a prolonged half-life (102.7 and 79.7 times to that in solution and in β-cyclodextrin, respectively) without any impact on the ROS production even after 16 hours of UVA irradiation. As a proof-of-concept, the photocatalytic degradation efficiency of FMN-POP complexes can be achieved at 58–93% against micropollutants under UVA. The stabilization of FMN by the "tail" capture in the POP allows its photocatalytic degradation function to be continuously online.

Environmental Implication: Porous organic polymer (POP)-decorated bacterial cellulose nanofibrous membrane (BCM) improves the photostability of flavin mononucleotide (FMN) by 100 times, allowing it to show constant production of reactive oxygen species under repeated light irradiations. The as-fabricated photosensitive material is promising for long-term photo-degradation of micropollutants in water stream. The combination of bio-based photosensitizer FMN with biodegradable fibrous substrate BCM provides a new approach of solving environmental pollution by an efficient, safe, lasting, and sustainable manner.

Graphical Abstract

*Corresponding author: gysun@ucdavis.edu (G. Sun).

CrediT authorship contribution statement

Dr. Peixin Tang: Conceptualization, Investigation, Data curation, Formal analysis, Investigation, Methodology, Validation and Writing-original draft; **Dr. Bolin Ji**: Data curation, Methodology, Validation and Writing-review & editing; **Dr. Gang Sun**: Conceptualization, Visualization, Supervision and Writing-review & editing.

Declaration of competing interest

Authors declare no conflict of interest.

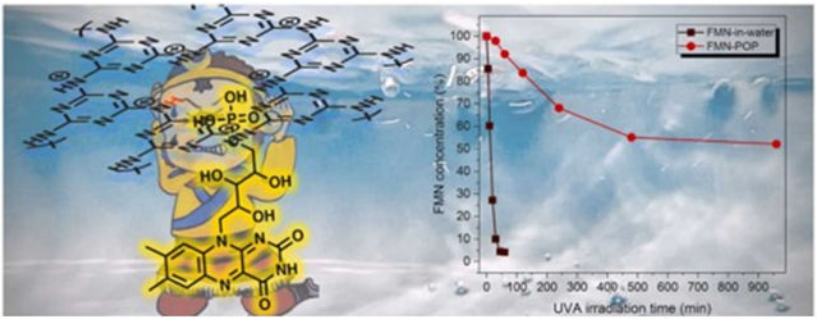

Keywords

Flavin; Host-guest system; Photocatalysis; Porous organic polymer; Water treatment

1. Introduction

With the rapid development of modern industries around the world, the occurrence of water pollutions caused by persistent organic compounds, including dyes, pesticides, pharmaceuticals, and plastic precursors, has posed concerns to the ecosystem and human health (Lu, et al., 2017; Quesada, et al., 2019). Although porous adsorbents with high specific surface area and micro/mesopores, such as activated carbons (Delgado, et al., 2019; Wang, et al., 2021), metal-organic frameworks (MOF) (Joseph, et al., 2019; Ma, et al., 2019), porous organic polymers (POP) (Alsbaiee, et al., 2016; Fan, et al., 2018), and zeolites (Jiang, et al., 2018; Vakili, et al., 2019) have been applied as adsorbents for wastewater treatments, challenges exist in the post-treatments of pollutant-contaminated slurries.

Photocatalytic degradation (shorted as photo-degradation) of micropollutants has attracted much attention in recent years because of the utilization of light as a renewable, easily available, and sustainable energy source (Gmurek, et al., 2017; Sahoo, et al., 2021). The usage of suitable photosensitizers (PS) could manipulate the requirement of high energy light (*e.g.,* ultraviolet light, 254 nm) to UV lights with longer wavelengths (e.g., UVA, 365 nm) or even in the visible range, making the photo-degradation process more economical and safer. The incorporation of PS onto a solid support is crucial to avoid secondary pollution from added PS and to make PS be recyclable and reusable. In this case, 3,3’,4’,4’-benzophenone tetracarboxylic dianhydride (Yi, et al., 2020), porphyrins (Neves, et al., 2019; Han, et al., 2021; Lyubimenko, et al., 2021), and rose Bengal-hybrid (Bielska, et al., 2015) were successfully incorporated onto fibrous materials and plastic films for efficient photo-degradation of different micropollutants. However, some of these PS possess potential toxicity despite their excellent photoactivity (Alharthi, et al., 2020; Lee, et al., 2021; Routoula and Patwardhan, 2020). Thus, the exploration of natural-derived PS and the investigation of their photocatalytic functions have become a promising research direction.

Riboflavin (Rf), also known as vitamin B_2, is a naturally derived photoactive compound that can be massively found in food. Its metabolite, flavin mononucleotide (FMN), is more promising in functional materials fabrication because of its good water-solubility. Due to no known safety concerns, FMN has a great potential to be used as a PS for water treatment.

Although FMN has been proved to be photoactive with the production of ROS, its fast self-degradation highly limited its practical use as an environmentally friendly, recyclable, and robust ROS generator for water treatments (Holzer, et al., 2005; Orsuwan, et al., 2019). The stability of FMN must be improved before it can be used as a naturally derived, green, and nontoxic PS in practical applications.

The self-degradations of flavin derivatives have been studied for more than thirty years (Rochette, et al., 2000; Schuman, et al., 1975; Insińska-Rak, et al., 2020). It was concluded that the intramolecular abstraction of hydrogens (H) from the ribityl side chain of FMN by their triplet excited states is the cause of its self-degradation (Schuman, et al., 1975; Insińska-Rak, et al., 2020). More importantly, this degradation process is governed by the free bending of the FMN molecules (Schuman, et al., 1975). The photostability of flavins could be improved by controlling the production of their triplet excited state, but their photo-reaction efficiency in water treatment was subsequently decreased as well (Huang, et al., 2004; Natera, et al., 2012; Cabezuelo, et al., 2021). Based on the mechanism of the self-degradation reaction, restraining the free bending of FMN by introducing molecular steric hindrance is considered as an alternative and effective approach in reducing and preventing the self-degradation of FMN. Porous organic polymers (POP) are materials with high specific surface area and unique micro/mesopores, which have shown excellent adsorption capacity and served as host molecular carriers of selected guest chemicals (Lu, et al., 2021). Thus, POP material could be a potential carrier to capture FMN and prevent its self-degradation hypothetically.

Herein, we propose for the first time to use a triazine-based POP structure as a carrier to capture the ribityl side chain of FMN. The formation of the FMN-POP complexes is expected to inhibit the self-degradation of FMN by restraining its free molecular bending because of the large steric hindrance from the POP. With the success of *in situ* growing POP particles on bacterial cellulose nanofibrous membrane (BCM), the inhibition of FMN self-degradation was retained and demonstrated on a flexible fibrous material. The FMN-POP complex on the BCM (FMN-POP@BCM) provides benefits for photocatalytic degradation of micropollutant with easy handling and recyclability compared with the relevant particles. As a proof-of-concept study, both FMN-POP particles and FMN-POP@BCM are employed to perform UVA-irradiated degradation to a span of micropollutants with various molecular sizes and charges. The significant improvement of FMN photostability as forming FMN-POP complex allows the photo-degradation function of such materials to be continuously online. These findings demonstrate the effectiveness of using POP to inhibit the FMN self-degradation and helping to achieve its long-term and repeated uses for wastewater treatments in a safer and greener manner.

2. Materials and methods

2.1 Chemicals

Flavin mononucleotide (FMN) and N, N’-dimethyl-4-nitrosoaniline (*p*-NDA) were purchased from Spectrum Chemicals & Laboratory Products (Gardena, CA, USA). Melamine, cyanuric chloride, 1-naphthol (NPT), 1-aminoanthraquinone (AAQ), bisphenol A (BPA), reactive blue 4 (RB4), methylene blue (MB), L-histidine, lumichrome, and

riboflavin (Rf) were purchased from Sigma-Aldrich (St. Louis, MO, USA). Bacterial cellulose nanofibrous membrane (BCM) was bought from ZHONGBC, Hainan Guangyu Biological Technology Co. Ltd. (Hainan, China). All solvents were purchased from Fischer Scientific (Waltham, MA, USA). All chemicals were used as received.

2.2 Synthesis of POP and *in situ* growth on bacterial cellulose nanofibrous membrane (BCM)

The synthesis of a triazine-based POP was carried out by following our previous protocol (Tang, et al., 2021). With a sufficient purge of N_2 gas into the synthesis system using a N_2 gas tank for 10 min, the overoxidation of the POP is avoided. The final POP particles show a white color, and the actual yield was weighted and calculated as 78.88%.

The *in situ* growth of POP on BCM (POP@BCM) followed the procedures reported previously with modifications (Tang, et al., 2021). Specifically, BCM (~0.5 g) was first immersed in dimethylacetamide (DMAc) for 24 h to process a solvent exchange since water in the membrane could induce the hydrolysis of cyanuric chloride and lower the grafting ratio of POP. Then, the resultant BCM was transferred into 100 mL DMAc containing 2.8 mmol of cyanuric chloride and 1 mL of Et_3N for BCM activation. This process lasted for 60 min at 0 °C in an ice-water bath. The activated membrane was then immersed in 100 mL dimethyl sulfoxide (DMSO) containing 5.6 mmol of melamine with 1 mL of Et_3N as the catalyst. An additional 2.8 mmol of cyanuric chloride in 20 mL of DMSO was added to the above system. The reaction was sealed after N_2 gas purging for 10 min, and then reacted at 150 °C for 24 h. The resultant POP@BCM was obtained by washing the material with DMSO, H_2O, and MeOH, and dried at 60 °C under vacuum for overnight. The grafting ratio was calculated based on the weight gain of the membrane as 92.03%.

2.3 Fabrication of FMN decorated POP particles (FMN-POP) and nanofibrous membranes (FMN-POP@BCM)

The assemble of FMN in POP particles and on POP@BCM was achieved through adsorption at room temperature. Different initial concentrations of FMN ranging from 50 mg/L to 1000 mg/L in distilled water were prepared. Around 200 mg of POP or POP@BCM was put into 30 mL FMN solution. At different adsorption time points, the residual concentration of FMN in the solution was collected and measured by a UV-vis spectrophotometer (Evolution 600, Thermo Fisher, USA) (the original solution was diluted by 10 times) based on a calibration curve of $y = 0.0014x+0.0004$, $R^2 = 0.9999$. The y is the absorbance intensity at 446 nm, and x is the concentration of FMN in a unit of mg L^{-1}. The FMN uptake on the POP and POP@BCM at adsorption equilibrium was measured by inductively coupled plasma mass spectrometry (ICP-MS), and the results are shown in Fig. S1a. The detailed ICP-MS testing procedures are shown in the following section. The time-dependent adsorption curves of FMN on the POP and POP@BCM were plotted by measuring the initial and residual FMN concentrations in the solutions at specific timepoint by using UV-vis spectrophotometer (Fig. S1b–c). The bright yellow FMN-POP particles and FMN-POP@BCM were dried at 60 °C under low pressure overnight.

2.4 Characterizations

The SEM images were captured by a Quattro ESEM (Thermo Fisher Scientific, MA, USA). All the samples were coated with a thin layer of gold (~10 nm) before SEM scanning. The diffuse reflectance UV-vis spectra were obtained by an Evolution 600 UV-vis spectrophotometer (Thermo Fisher Scientific, MA, USA). N_2 adsorption-desorption isotherms were obtained from a physisorption system of ASAP 2020 (Micromeritics Co., GA, USA). The samples were de-gassed at 60 °C for 4 h before testing. The Brunauer-Emmett-Teller (BET) surface areas and porous structures were calculated according to BET and Horvath-Kawazoe (HK) theory models. ^{1}H NMR spectra were collected using a Bruker 400 MHz NMR spectrometer (MA, USA). Deuterium oxide and deuterium chloroform were used as the solvents. The fluorescence spectra of FMN-in-water and FMN-POP suspensions were collected in a SpectraMax ID5 spectrometer (Molecular Devices CA, USA) with an excitation wavelength at 365 nm. The spectra were acquired in the range of 400–700 nm. The sample was prepared by dispersing different amounts of POP particles in 10 mL 100 mg L^{-1} FMN solutions and incubated under dark at room temperature for 24 h to ensure the capture of FMN by POP reached equilibrium. ICP-MS results were acquired in an Agilent 7500a ICP-MS (Agilent Technologies Inc., CA, USA) after a microwave digestion treatment with a CEM Mars6 Microwave reactor (CEM Co., NC, USA). Specifically, precisely weighted (100 mg) samples were treated by 10 mL of concentrated HNO_3 and were brought up to a final volume of 20 mL with MilliQ water, resulting in clear solutions. The microwave digestion program was performed by heating the system to 200 °C within 15 min and holding at 200 °C for another 15 min with digestion power of 1800W.

2.5 Measurement of FMN and lumichrome

The concentration of FMN in solution was directly measured using the UV-vis spectrophotometer. Its concentration in the FMN-POP particles and FMN-POP@BCM was extracted by 10 mL of 0.02 M NaOH overnight. The extracted solution was measured by recording the UV-vis absorbance intensity at 446 nm. On the other hand, the quantification of lumichrome in/on different systems, including FMN solution, FMN-POP, and FMN-POP@BCM, was performed using chloroform as the extraction solvent. For solution samples, 1.5 mL of chloroform was added into 1 mL of sample solution, and the mixture was vortexed vigorously for 30 s. In the case of membrane samples, 10 mL of chloroform was used to wash the tested membrane under vortex for 30 s. Then, the chloroform layer was collected for UV-vis measurements in quartz cuvettes. The concentration of lumichrome was calculated based on a calibration curve of $y = 0.0217x+0.0074$, $R^2 = 0.9988$, where y is the absorbance intensity at 352 nm, and x is the lumichrome concentration in a unit of mg L^{-1}. The calibration curve was obtained by preparing a serial of lumichrome standard solutions in chloroform. The UV-vis spectra fit of standard lumichrome in chloroform, and chloroform extracted photolysis product are shown in Fig. S2.

2.6 Measurement of ROS

The measurements of hydroxyl radical (HO•) and singlet oxygen ($^1O_2$) were achieved by using *p*-NDA and *p*-NDA/$_L$-histidine solutions prepared in phosphate-buffered saline (PBS, pH = 7.4), respectively (Zhang, et al., 2019; Zhang, et al., 2021). The light source was

provided by a Spectrolinker™ 1500-XL crosslinker box (Spectronics Co., NY, USA) with six 15 W UVA bulbs. The UVA intensity was measured as 30 W m^{-2} by an Ultra-Violet radiometer (Fisher Scientific, MA, USA). FMN-POP particles or FMN-POP@BCMs were weighted as around 20 mg in a 20 mL glass vial. Then, 10 mL of 40 μM *p*-NDA or 120 μM/0.10M *p*-NDA/$_L$-histidine solutions were added to the vial. The vials were exposed to light for a specific duration, and the residual concentrations of *p*-NDA were determined by UV-vis spectroscopy based on a calibration curve of y = 0.3387x-0.0095, R^2 = 0.9998. Where y is the absorbance intensity at 430 nm, x is the concentration of *p*-NDA (10^{-5} M). The bleaching of *p*-NDA is mainly attributed to HO• production, while the co-existence of HO• and $^1O_2$ causes the bleaching of *p*-NDA/$_L$-histidine system. The generation of $^1O_2$ in the system was determined based on the *p*-NDA consumption difference between the *p*-NDA and *p*-NDA/$_L$-histidine systems. It is important to note that after 30-min of UVA irradiation, all *p*-NDA in the *p*-NDA/$_L$-histidine system was consumed by produced $^1O_2$ from FMN-POP particles, so the $^1O_2$ measurement (i.e., from 30 min to 90 min) was continued by transferring the particles to another 10 mL of *p*-NDA/$_L$-histidine solution. Since the FMN-in-water system could not be recycled, the measurement of its $^1O_2$ production was only tested for 45 min until all *p*-NDA was consumed.

H_2O_2 was quantified based on the oxidation of potassium iodide (Zhang, et al., 2021). Specifically, solution A was prepared with 66 g L^{-1} potassium iodide, 2 g L^{-1} sodium hydroxide, and 0.2 g L^{-1} ammonium molybdate tetrahydrate in distilled water. Solution B was made by dissolving 20 g L^{-1} potassium hydrogen phthalate in distilled water. During the test, 20 mg of FMN-POP or FMN-POP@BCM was immersed in 10 mL of distilled water in a 20 mL glass vial and exposed to light for different durations. At each testing time point, 1 mL of the sample solution was collected and mixed with 1 mL of solution A and 1 mL of solution B. The mixture was shaken in dark for 5 min before the UV-vis spectroscopy test. The produced H_2O_2 (μM) was quantified by recording the absorbance intensity at 350 nm and calculated based on a calibration curve of y = 0.0094x+0.0187, R^2 = 0.9993.

The relative quantum yield of $^1O_2$ of FMN-in-water and FMN-POP complex were measured by using rose Bengal as a benchmark photosensitizer (Paczkowski, et al., 1985). The concentration of rose Bengal, FMN both in water and in FMN-POP were controlled as 5 mg L^{-1}. The relative quantum yield was calculated based on the consumption amount of 10 mL 60 μM *p*-NDA by generated $^1O_2$ from per mole of photosensitizer after 10 min of UVA irradiation.

2.7 Photocatalytic degradation studies

Photocatalytic degradation studies were performed in 20 mL glass vials. In studies involving POP, FMN-POP and FMN-POP@BCM, the materials (20 mg) were incubated with 10 mL of 0.1 mM pollutants in the XL-1500 crosslinking box equipped with six 15 W UVA (365 nm) bulbs (UVA intensity = 30 W m^{-2}). The initial concentrations of the pollutants were much higher than the environmentally relevant values to ensure the photocatalytic efficacy of FMN-POP complexes for real applications (Alsbaiee, et al., 2016; Oulton, et al., 2010). The direct photo-degradations of pollutants were performed under the same condition without addition of materials as controls. After a specific light irradiation duration,

1 mL of solution was collected and scanned in the UV-vis spectrophotometer for residual concentration determinations of BPA, MB (diluted by 10 times), and RB4. Given the turbid solutions of NPT and AAQ, 1.5 mL of chloroform was vortexed with 1 mL of the sample solution for 30 s. Then, the chloroform phase was collected for pollutant concentration determination by UV-vis spectroscopy. The calibration curves and limit of detection (LOD) of each pollutant are summarized in Table S1.

The efficiency of pollutant photo-induced degradation (in %) was determined according to Equation (1).

$$Degradation\ efficiency = \frac{C_0 - C_t}{C_0} \times 100\,\% \quad (1)$$

Where C_0 (mM) and C_t (mM) stand for the pollutant concentrations before and after photo-degradation, or physical adsorption under the dark condition.

2.8 Computational calculations

All theoretical calculations, including ground-state structure optimization and frequency calculation, were performed with Gaussian 09 at unrestricted DFT-B3LYP/6-311G(d,p) level of theory. The UV-vis spectra were predicted based on the TD-DFT-B3LYP/6-311G(d,p) level of theory under vacuum or in H_2O system. The HOMO and LUMO orbital images were obtained based on optimized geometries and viewed by GaussView 5.0.

3. Results and discussion

3.1 Fabrication of FMN-POP complex and its stabilization function

In this study, the term of “self-degradation” is used to describe the degradation of FMN under light treatment, while the “photocatalytic degradation” or “photo-degradation” stands for the removal of micropollutants under light treatment. With an energy input (e.g., light irradiation), there is a trend to convert FMN from an unfolded geometry to a folded one (Fig. 1a), making the intramolecular H-abstraction and subsequent self-degradation “sterically” allowed. The POP synthesized from cyanuric chloride and melamine possesses cationic feature, ultrahigh specific surface area (S_{BET} = 1843.35 $m^2\ g^{-1}$), micropores (pore width = 0.783 nm), and large pore volumes (2.023 $cm^3\ g^{-1}$), making it a structural stabilizer of FMN via formation of a complex structure (see detailed characterizations of POP and its related materials including FMN-POP particles, POP@BCM, and FMN-POP@BCM in the Supplementary Material in Fig. S3–S10). Considering the pore size fit, the capture of FMN by POP driven by electrostatic-driven guest-host interaction could be achieved by filling the POP micropores by the ribityl side chain (i.e., the “tail”) of FMN (Fig. 1b and Fig. S9). In this case, the large molecule of POP restricts the movement (such as the bending back) of the isoalloxazine ring (i.e., the FMN’s “head”), thus sterically inhibiting intramolecular H-abstraction and self-degradation. Here, the microporous POP behaves like a magic golden fillet of monkey king described in the popular Chinese classic novel named *The Journey to the West* (Fig. 1b). Proved by experimental results, FMN dissolved in the

water system (FMN-in-water) was unstable under ultraviolet light (UVA, 365 nm) exposure. The concentration of FMN in water dropped quickly within minutes and almost disappeared after 45 min of light exposure. The degradation of FMN can be plotted according to the first-order kinetics with a rate constant (k_d) of 0.074 min^{-1}. The fast decomposition of FMN was also found under daylight exposures (k_d = 0.0178 min^{-1}) or nitrogen atmosphere (k_d = 0.0585 min^{-1}) (Fig. S11 and Table S2). On the contrary, the degradation of FMN in POP (FMN-POP) could almost be ignored within hours of UVA irradiations. With prolonging the UVA irradiation time to 16 h, the FMN can still be retained around 55% (Fig. 1c). The FMN self-degradation rate constant, in this case, was plotted as 0.00072 min^{-1}, and its stability has been improved by 102.7 times. The capture of FMN in POP successfully extended the half-life of FMN from 9.37 min to 16.05 h (Fig. 1c and Table S2). Given the self-degradation mechanism of FMN (Schuman, et al., 1975), the H-donating function of POP could also play an essential role in the photo-stability of FMN by replacing the H-donation potential of the FMN side chain (Tang, et al., 2021). To further understand the stabilization mechanism, the H-donor sites in the POP were purposely consumed by reacting with methyl iodide (MeI) (Fig. S12a–b). The photo-stability of FMN in the FMN-POP-MeI_x (x refers to the volume of MeI injected and incubated with the FMN-POP particles for 24 h) was even improved than that of the FMN-POP, with more than 70% FMN retained after 16 h of UVA irradiation (Fig. S12c). This improved stability is caused by the decreased ROS production from the FMN-POP-MeI_x system due to the loss of H-donors from POP (Fig. S12d), which is consistent with our previous results and the literature (Huang, et al., 2004; Natera, et al., 2012; Tang, et al., 2021). Thus, the stabilization mechanism of the FMN-POP complex has been proved as the restraining effect on the FMN bending provided by the “magic golden fillet” of POP rather than its H-donor feature.

The major product of the self-degradation of FMN, lumichrome, can be easily detected from FMN-in-water system after 5 min of UVA treatment. By increasing the light irradiation time, the concentration of lumichrome in the system increased to 212.31 μmol L^{-1} at 30 min and slightly decreased as further prolonging the photo-irradiation to 60 min. The decrease of lumichrome production could be caused by the decomposition of lumichrome by the generated ROS from FMN. Interestingly, the production of lumichrome was comparable to the initial concentration of FMN (250 μmol L^{-1}), confirming that lumichrome is the major product of the FMN self-degradation. The side products can contain lumiflavin and others (Holzer, et al., 2005). However, the addition of POP in the FMN system significantly inhibited the self-degradation of FMN. The inhibition effect was enhanced by increasing the molar ratio of POP: FMN from 0:1 to 26.0:1, resulting from that more FMN molecules were able to be captured by the POP. When the POP: FMN ratio reached 10.4:1 or 26.0:1, the production of lumichrome became negligible during the testing period. It can also be estimated that each FMN molecule was captured by a space constructed by tens of layers of POP repeating rings (i.e., been built by six triazine rings connected by secondary amines).

Interestingly, the fluorescence of FMN has been quenched when the FMN-POP complex was formed. As shown in Fig. 1e, increasing the molar ratio of POP: FMN, the fluorescence intensity dropped accordingly from 3.15×10^8 to 8.40×10^5, which further indicated the complex formation between FMN and POP. The fluorescence quenching in the FMN-POP complex is a result of photo-induced electron transfer (PET) effect as that FMN and POP

worked as an electron acceptor and an electron donor, respectively (Rhee, et al., 2009). This interaction can be experimentally proved by matching the electrochemical properties of POP and FMN according to the reported experimental results (Xue, et al., 2018; Xie, et al., 2020; Leonat, et al., 2013). The HOMO and LUMO energy levels of POP and FMN were reported as –4.155 eV and –4.900 eV, respectively, making the electron transfer from POP to FMN allowed. Additionally, the electron transfer between POP and FMN was predicted via the density functional theory (DFT) (Fig. 1f and Fig. S13). The predicted result shows a characteristic absorbance at 353.55 nm, which refers to the intermolecular electron transfer from the triazine-N in POP (HOMO-1 orbital of the FMN-POP complex) to the isoalloxazine ring of FMN (LUMO orbital of the complex) (Fig. 1g). On the other hand, the absorbance of FMN at 429.57 nm, which is attributed to the intramolecular electron transfer of the isoalloxazine ring (i.e., n_{HOMO}–π^*_{LUMO}), kept constant in the FMN-POP complex, ensuring no impact on photoactivity of FMN. The FMN characteristic peaks at 371 nm and 445 nm undergo a redshift to 383 nm and 467 nm in FMN-POP, respectively, which further proved the intermolecular interaction between FMN and POP. The photo-induced excitation process of FMN molecule was also predicted under DFT, and the results are summarized in Fig. S14–S16.

To get a concrete insight into the complex geometry of FMN-POP, several tests have been conducted. Based on the cationic feature of POP under acidic and neutral conditions (see Zeta potential results in Fig. S8), the interaction between POP and FMN (mainly on the “tail” end) can be governed by an electrostatic interaction, and an alkaline solution could break this connection. As a result, 76% of the FMN can be washed off from the FMN-POP particles by 0.02 M NaOH solution. Secondly, the stabilization effect of POP toward Rf (vitamin B_2) was examined. Due to the lack of anionic groups in Rf, its photostability in the POP complex can only be improved by 7.74 times compared with that in the solution (Fig. S17 and Table S3). Moreover, β-cyclodextrin (β-CD), a popular natural-based adsorbent with a hydrophobic cavity (pore width = 0.60–0.65) (Saenger, 1980), was used to capture FMN, and the photostability of the complex was tested for comparison. With a molar ratio of β-CD: FMN = 10.4: 1, the self-degradation of FMN could not be highly improved, which degradation rate constant was examined as 0.0574 min^{-1} and the half-life only increased to 12.08 min, respectively. The fourth strategy was conducted by comparing the uptakes of FMN and lumichrome on POP. Because the lack of an anionic “tail” in lumichrome structure, the molar uptake of lumichrome was only one-third to that of the FMN, which is consistent with the removable amount of FMN in alkaline solutions. Here, the adsorption of lumichrome is mainly due to the π–π stacking from the ultrahigh specific surface area of POP.

In conclusion, the capture of FMN in POP is dominated by the interaction between the anionic “tail” in FMN and the cationic POP, and the complex structure restrains the free bending back of the “head” to undergo the intramolecular H-abstraction from the “tail” (Fig. 1b).

The photocatalytic production of ROS, including hydrogen peroxide (H_2O_2), HO•, and $^1O_2$ by FMN-in-water and FMN-POP was examined under the UVA irradiation. As shown in Fig. 2a, the production of H_2O_2 from the FMN-in-water was initially higher than that of the

FMN-POP particles (i.e., from 0 to 30 min), but no more production was noticed afterward. The production of H_2O_2 from FMN-POP particles kept linearly increasing with prolonging the irradiation time. The generation of HO• from the FMN-in-water and the FMN-POP particle showed a comparable increasing trend under the UVA irradiation (Fig. 2b). The continuous growth of HO• from the FMN-in-water could be caused by the decomposition of pre-generated H_2O_2 in the system. In addition, the production of $^1O_2$ was monitored, and the results are shown in Fig. 2c. Similar to the trend of H_2O_2 generation, the production of $^1O_2$ from the FMN-in-water reached the maximum after 10 min of light irradiation, but the FMN-POP particles could continuously produce $^1O_2$ (Fig. 2c). According to the poor FMN photostability in solution (Fig. 1c–d), its photodegraded products (i.e., lumichrome) could also contribute to the generation of $^1O_2$ during the measurement. Lumichrome was reported as a good $^1O_2$ producer with a quantum yield of 0.85 in methanol (Sikorska, 2004), while this value for FMN was only 0.51 (Baier, et al., 2006). Comparing the generation amounts of HO• and $^1O_2$, the type II photoreaction (i.e., performing $^1O_2$ production) of FMN either in solution or in POP is dominant over the type I (i.e., production of H_2O_2 and HO•). Surprisingly, the constant production of sufficient amounts of ROS was observed by UVA-aged FMN-POP particles, even after 16 h of UVA-irradiations (Fig. S18). Given the excellent photostability, FMN-POP particles exhibited continuous photocatalytic production of ROS, allowing such materials capable for green, robust, and long-term photo-degradations of environmental micropollutants.

Comparing to the production of $^1O_2$ by rose Bengal, which is a well-accepted benchmark photosensitizer with a known $^1O_2$ quantum yield in water (φ=0.75) (Paczkowski, et al., 1985), the relative $^1O_2$ quantum yields of FMN-in-water and FMN-POP particles can be obtained (Fig. 2d). The measured relative quantum yield of FMN (φ=0.569) is slightly lower than that of the rose Bengal. The decreased quantum yield of FMN-POP particles (φ=0.430) could be caused by its water insolubility. The macroscale aggregation of FMN-POP particles could cause a self-quenching effect, which can be ignored in the case of FMN-in-water.

3.2 Incorporation of FMN-POP complex on BCM

By *in situ* growing POP on BCM, the inhibition of the FMN self-degradation of the complex system could also be achieved on a flexible fibrous material, making applications of such materials in photocatalytic decontamination of water practical and feasible. Taking the same chemistry that was applied in growing POP on cotton fibers (Tang, et al., 2020), POP was homogeneously grafted on the BCM. The SEM and BET results proved the homogenous growth of POP on the BCM, thus allowing the POP@BCM to possess a high specific surface area (S_{BET} = 255.52 $m^2\ g^{-1}$) and massive porosity (pore volume = 0.743 $cm^3\ g^{-1}$) (Fig. S3). As a comparison, FMN was adsorbed on a quaternary ammonium salt modified BCM (Cationic@BCM), and its modification process is available in the in the Supplementary methods and Fig. S19. The Cationic@BCM can provide the desired electrostatic interactions between the cationic cellulose and anionic FMN but without the “magic golden fillet” capturing function on the ribityl side chain of FMN. Under SEM imaging, the uniform growth of nanosized POP on the BCM enlarged the fiber diameter of POP@BCM from 68.03±16.62 nm to 107.53±20.20 nm, while the Cationic@BCM showed minor changes to the fiber morphology and diameter (Fig. 2a and

Fig. S20). The incorporation of FMN on POP@BCM and Cationic@BCM was achieved by physical adsorption at room temperature (see FMN uptake results in Fig. S1). Firstly, the photostability of FMN on the two types of membranes (i.e., FMN-POP@BCM and FMN-Cationic@BCM) were examined by performing diffuse reflectance UV-vis spectra (DRS) according to different UVA irradiation times. The fast degradation of FMN on Cationic@BCM can be noticed after 5 min of light exposure, presenting a drop of peak intensity of FMN at 450 nm (Fig. 3b–c). The peak intensity of FMN-POP@BCM also decreased but retaining its peak pattern in the range of 330–600 nm. To get an insight into the chemical component changes on these two membranes after UVA irradiation, different solvents were used to extract specific compounds from the membranes for identification and quantification. In detail, FMN residues on the membranes were washed off by 0.02 M NaOH solution, while chloroform was used to extract photodegraded products from the solution. As summarized in Fig. 3d, the concentration change of FMN on two membranes was consistent with the DRS results. The FMN content on the Cationic@BCM dropped in the first 5 min and continuously decreased to around 35% of its original concentration after 60 min of UVA irradiation, whereas the loss of FMN on the POP@BCM was much slower, presented around 70% FMN retention after 60 min of UVA irradiation. On the other hand, the produced lumichrome can only be detected on the FMN-Cationic@BCM, while no detectable lumichrome was found on the FMN-POP@BCM (the detection limit of lumichrome from UV-vis spectroscopy was tested as 0.045 μM).

The above phenomenon triggered us to investigate the slight decrease of the absorbance on FMN-POP@BCM under the UVA irradiation. According to the photoreaction diagram of flavins illustrated in Fig. 3f, the triplet excited state of FMN can abstract H from its surrounding H-donors to generate its reduced form, flavin semiquinone, which shows a decreased absorbance intensity, specifically in the visible range (~400 nm), than the parent FMN. The reduced form of FMN can be converted back to FMN after interactions with sufficient O_2, which ensures the regeneration of FMN for photocatalytic water degradations. The generation of reduced FMN (i.e., flavin semiquinone) can also be noticed from the DRS results as a peak gradually appeared around 300 nm, which was proved by the DFT calculation (S_2, 282.65 nm) (Fig. S21).

The continuous production of ROS on the FMN-POP@BCM is essential to be monitored. As shown in Fig. 3g–i, the generation of type I and type II ROS was quantified for six cycles (each cycle lasted 60 min). Given the stabilization function of POP, the FMN-POP@BCM can continuously produce all three types of ROS in each cycle. Since the occurrence of type I and type II photoreactions is always competitive, both consuming the triplet excited state of FMN, the close position of FMN to POP (i.e., good H-donors) in the complex could favor the type I reaction and result in the constant production of H_2O_2 and HO• as the UVA irradiation time is increased. Aging of the materials is shown by the gradual decrease of the $^1O_2$ production (Fig. 3i). However, the FMN-Cationic@BCM was only able to sufficiently generate ROS in the first cycle. In other words, the FMN-Cationic@BCM is only suitable for one-time use due to the self-degradation of FMN, while FMN-POP@BCM could continuously provide the photocatalytic micropollutant degradation for a longer duration.

3.3 Micropollutants removal and photo-degradation

The fabrication processes of FMN-POP and FMN-POP@BCM and their applications on micropollutant photo-degradation are exhibited in Scheme 1. The ultra-high specific surface area and permanent porosity of POP structures enable the massive and stable uptake of FMN in the resultant materials for efficient and continuous production of ROS under light irradiation. Meanwhile, the high specific surface area of the FMN-POP@BCM also provides adsorption sites to interact with pollutants, which is crucial to the photo-degradation efficiency achieved by the short-lived ROS. The photo-degradation functions of FMN-POP particles and FMN-POP@BCM were examined by challenging the materials with a span of micropollutants in aqueous solutions, including endocrine disruptor, organic dyes, pesticide metabolites, and aquatic hazards (Fig. 4a). Specifically, bisphenol A (BPA) is an endocrine disruptor from plastic products; methylene blue (MB) and reactive blue 4 (RB4) are cationic and anionic dyes that were applied as medication and in textile industries; 1-naphthol (NPT) is a metabolite from insecticides of carbaryl and naphthalene; and 1-aminoanthraquinone (AAQ) is a colorant used in drugs, textiles, and food but toxic to aquatic lives. The FMN loading amount of 34.21 mg g^{-1} on the complexes was selected based on the ROS production and the degradation efficiency toward RB4 as a pollutant representative (Fig. S22 and S23). Under UVA irradiation, both FMN-POP particles and FMN-POP@BCM showed 58–93% removals of the parent compounds (synergistic effect of photo-degradation and physical adsorption) of all tested pollutants from the water system within 180 min. However, the removals of these pollutants either with POP under UVA irradiation (Fig. S24) or with FMN-POP under dark condition (Fig. 4c and 4e) presented slower rates and lower uptakes, revealing the essential role of ROS produced by FMN complexes in facilitating micropollutant photo-degradation. It is also worth to note that the self-degradation of the pollutants under UVA irradiation can be ignored compared with the clean-up efficiency that was achieved under FMN-POP photocatalysis scenario. Although the intrinsic production of ROS by MB is well-known, the MB self-degradation under UVA only reached to 20% (Fig. S24). The optical images of the samples under photocatalytic degradation by the FMN-POP@BCM are shown in Fig. S25. Meanwhile, negligible FMN leaching from the complexes was found under acidic and neutral conditions and different temperatures, which ensured the material stability under the environmentally relevant and wide-scale conditions (Fig. S26).

In addition, different photo-degradation rates and efficiencies could be noticed among all tested compounds, which were highly related to their molecular sizes and charges. The efficiency difference was more evident by using FMN-POP@BCM as the photo-degradation material (Fig. 4d). For instance, the rates of detoxifying neutral compounds are mainly determined by the size (predicted from DFT calculation) and the conjugation complexity (evaluated by the degree of unsaturation (DoU)) of the molecules (Table S4). The photo-degradation of the simplest NPT was most efficient and followed by that of BPA and AAQ, which possess similar molecular sizes, yet the latter one has a more extensive conjugated system. The charges on the pollutants also play an essential role in controlling the photo-degradation performance of the materials. RB4 is an anionic dye, while MB contains a positive charge, which led to different degradation efficiency. The electrostatic interaction between anionic RB4 and cationic POP allowed more physical uptakes and close contact of

RB4 with the detoxifying material surfaces, where the reactive and short-lived ROS were densely produced and efficiently functioning. In this case, the photo-degradation efficiency of RB4 by the FMN-POP@BCM could be achieved as 88.88%, in the second place among five tested pollutants, even though that its large molecular size could limit the adsorption kinetics and uptake capacity to some degree (Table S4). Under the dark condition, around 60% of RB4 was adsorbed on the FMN-POP@BCM. On the contrary, the electrostatic repulsion between POP and MB resulted in slower and less efficient photo-degradation of MB, with photo-degradation efficiencies achieved at 79.83% and 56.54% on FMN-POP particles and FMN-POP@BCM, respectively (Fig. 4b–e). The weakest adsorption ability of the materials toward AAQ is because of its low water solubility. In conclusion, the photo-degradation efficiencies of FMN-POP particles and FMN-POP@BCM membrane against pollutants are highly related to the physicochemical properties of the target chemicals.

We employed ^{1}H NMR to check the chemical components in the system after photo-degradation. The decrease or disappearance of characteristic peaks of pollutants can be noticed (Fig. S27). Given the efficient and continuous production of ROS, the photo-degradation of the micropollutants could reach the mineralization step (*i.e.,* converting parent compounds to CO_2 and H_2O), making the degraded concentrations of intermediates lower than the detection limit in the ^{1}H NMR. On the other hand, the massive porosity and high specific surface area of FMN-decorated materials could retain degraded intermediates in the treated water by physical adsorption. Although the analysis of degraded products is not the focus of this work, more detailed analysis of the treated water should be addressed in the future to understand their photo-degradation pathways when the FMN-POP materials are employed in water treatments. Fortunately, the structures of ROS-triggered degraded products of BPA, MB, naphthalenes, and anthraquinone dyes have already been reported elsewhere (Lee and Lane, 2009; Liu and Sun, 2011; Tsai, et al., 2009; Da Silva, et al., 2014; Khataee, et al., 2011).

Unlike FMN-POP particles, recycle and reuse of the FMN-POP@BCM are much easier and more convenient to handle without material loss between each application cycle. Herein, the repeated uses of FMN-POP@BCM for NPT photo-degradation were performed to demonstrate the application robustness of such materials (Fig. 4f). During the first UVA irradiation cycle, 92.20% of NPT was removed by the membrane within 60 min. After seven application cycles, the FMN-POP@BCM could still degrade 62.5% of NPT within 60 min. The decrease of the photo-degradation efficiency during the long-term use could be attributed to the partial occupancy of the adsorption sites by previously adsorbed NPT or its degraded products, which limited the close contact between additional NPT and the short-lived ROS, or the decreased generation of $^{1}O_2$. This conclusion was evidenced by the fact of a constant production of ROS except for $^{1}O_2$ but a decreased adsorption ability of FMN-POP@BCM after seven cycles of NPT photo-degradation (Fig. 2 and S28).

4. Conclusion

In summary, we fabricated a cationic POP to capture the “tail” of photoactive FMN, achieving controlled self-degradation of FMN under UVA irradiation, by avoiding the intramolecular H-abstraction via FMN free bending restriction. The geometry of FMN-POP

complex has been proved via experimental and theoretical studies. The stabilization effect of POP successfully improved the photoactivity of FMN by 102.7 times in terms of FMN's half-life (962.70 min vs. 9.7 min) and the self-degradation rate constant (0.00072 min^{-1} vs. 0.074 min^{-1}) with efficient and constant ROS production. Applying this strategy, we developed highly efficient and robust photocatalytic materials, including FMN-POP particles and FMN-POP@BCM membranes, for water purification. The improved stability of FMN in such materials ensured the use of FMN as a sustainable, green, and nontoxic photosensitizer for repeated and long-term water treatment, making the photo-degradation function continuously online.

Supplementary Material

Refer to Web version on PubMed Central for supplementary material.

Acknowledgments

This work was financially supported by the National Institute of Environmental Health Sciences (NIEHS), USA (Grant No. 5P42ES004699). The ThermoFisher Quattro ESEM was funded through the US National Science Foundation (Grant No. DMR-1725618). The authors would like to thank Dr. Yue Ma, Mr. Bofeng Pan, Mr. Huitao Ling, Ms. Mingyuan Wang, and Dr. Austin Cole (UCD Interdisciplinary Center of Plasma Mass Spectrometry) at the University of California Davis, CA, USA for helping to collect the EDS, fluorescence spectra, ^{1}H NMR, PXRD, and ICP-MS, respectively. The authors are also grateful to Chuhan Luo (*The Monkey King* picture credit), Jialin Li, Junhua Zhu, and Zhihui Yao, the sixth-grade students at Lequn Elementary School, Guilin, Guangxi, China, for their wonderful ideas and drawings of Monkey King displayed in this work.

References

Alharthi FA; Alghamdi AA; Alanazi HS; Alsyahi AA; Ahmad N Photocatalytic Degradation of the Light Sensitive Organic Dyes: Methylene Blue and Rose Bengal by Using Urea Derived g-C3n4/Zno Nanocomposites. Catalysts 2020, 10 (12), 1–16. 10.3390/catal10121457.

Alsbaiee A; Smith BJ; Xiao L; Ling Y; Helbling DE; Dichtel WR Rapid Removal of Organic Micropollutants from Water by a Porous β-Cyclodextrin Polymer. Nature 2016, 529 (7585), 190–194. 10.1038/nature16185. [PubMed: 26689365]

Baier J; Maisch T; Maier M; Engel E; Landthaler M; Bäumler W Singlet Oxygen Generation by UVA Light Exposure of Endogenous Photosensitizers. Biophys. J 2006, 91 (4), 1452–1459. 10.1529/biophysj.106.082388. [PubMed: 16751234]

Bielska D; Karewicz A; Lachowicz T; Berent K; Szczubiałka K; Nowakowska M Hybrid Photosensitizer Based on Halloysite Nanotubes for Phenol-Based Pesticide Photodegradation. Chem. Eng. J 2015, 262, 125–132. 10.1016/j.cej.2014.09.081.

Cabezuelo O; Martinez-Haya R; Montes N; Bosca F; Marin ML Heterogeneous Riboflavin-Based Photocatalyst for Pollutant Oxidation through Electron Transfer Processes. Appl. Catal. B Environ 2021, 298, 120497. 10.1016/j.apcatb.2021.120497.

Da Silva JCC; Reis Teodoro JA; De Cássia Franco Afonso RJ; Aquino SF; Augusti R. Photodegradation of Bisphenol A in Aqueous Medium: Monitoring and Identification of by-Products by Liquid Chromatography Coupled to High-Resolution Mass Spectrometry. Rapid Commun. Mass Spectrom 2014, 28 (9), 987–994. 10.1002/rcm.6863. [PubMed: 24677519]

Delgado N; Capparelli A; Navarro A; Marino D Pharmaceutical Emerging Pollutants Removal from Water Using Powdered Activated Carbon: Study of Kinetics and Adsorption Equilibrium. J. Environ. Manage 2019, 236, 301–308. 10.1016/j.jenvman.2019.01.116. [PubMed: 30738300]

Fan H; Gu J; Meng H; Knebel A; Caro J High-Flux Membranes Based on the Covalent Organic Framework COF-LZU1 for Selective Dye Separation by Nanofiltration. Angew. Chemie - Int. Ed 2018, 57 (15), 4083–4087. 10.1002/anie.201712816.

Gmurek M; Foszpańczyk M; Olak-Kucharczyk M; Gryglik D; Ledakowicz S Photosensitive Chitosan for Visible-Light Water Pollutant Degradation. Chem. Eng. J 2017, 318, 240–246. 10.1016/j.cej.2016.06.125.

Han J; Zhu Z; Li N; Chen D; Xu Q; Li H; He J; Lu J Metalloporphyrin-Based D-A Type Conjugated Organic Polymer Nanotube for Efficient Photocatalytic Degradation. Appl. Catal. B Environ 2021, 291, 120108. 10.1016/j.apcatb.2021.120108.

Holzer W; Shirdel J; Zirak P; Penzkofer A; Hegemann P; Deutzmann R; Hochmuth E Photo-Induced Degradation of Some Flavins in Aqueous Solution. Chem. Phys 2005, 308 (1–2), 69–78. 10.1016/j.chemphys.2004.08.006.

Huang R; Choe E; Min DB Kinetics for Singlet Oxygen Formation by Riboflavin Photosensitization and the Reaction between Riboflavin and Singlet Oxygen. J. Food Sci 2004, 69 (9), 726–732. 10.1111/j.1365-2621.2004.tb09924.x.

Insińska-Rak M; Prukała D; Golczak A; Fornal E; Sikorski M Riboflavin Degradation Products; Combined Photochemical and Mass Spectrometry Approach. J. Photochem. Photobiol. A Chem 2020, 403, 112837. 10.1016/j.jphotochem.2020.112837.

Jiang N; Shang R; Heijman SGJ; Rietveld LC High-Silica Zeolites for Adsorption of Organic Micro-Pollutants in Water Treatment: A Review. Water Res. 2018, 144, 145–161. 10.1016/j.watres.2018.07.017. [PubMed: 30025266]

Joseph L; Jun BM; Jang M; Park CM; Muñoz-Senmache JC; Hernández-Maldonado AJ; Heyden A; Yu M; Yoon Y Removal of Contaminants of Emerging Concern by Metal-Organic Framework Nanoadsorbents: A Review. Chem. Eng. J 2019, 369, 928–946. 10.1016/j.cej.2019.03.173.

Khataee AR; Zarei M; Fathinia M; Jafari MK Photocatalytic Degradation of an Anthraquinone Dye on Immobilized TiO2 Nanoparticles in a Rectangular Reactor: Destruction Pathway and Response Surface Approach. Desalination 2011, 268, 126–133. 10.1016/j.desal.2010.10.008.

Lee JY; Lane DA Unique Products from the Reaction of Naphthalene with the Hydroxyl Radical. Atmos. Environ 2009, 43 (32), 4886–4893. 10.1016/j.atmosenv.2009.07.018.

Lee YM; Lee G; Zoh KD Benzophenone-3 Degradation via UV/H2O2 and UV/Persulfate Reactions. J. Hazard. Mater 2021, 403, 123591. 10.1016/j.jhazmat.2020.123591. [PubMed: 32795823]

Leonat L; Sbârcea G; Brañzoi IV Cyclic Voltammetry for Energy Levels Estimation of Organic Materials. UPB Sci. Bull. Ser. B Chem. Mater. Sci 2013, 75 (3), 111–118.

Liu N; Sun G Photo-Degradation of Methylene Blue in the Presence of 2-Anthraquinone Sulfonate and Cyclohexanol. Dye. Pigment 2011, 91 (2), 215–224. 10.1016/j.dyepig.2011.03.018.

Lu GH; Gai N; Zhang P; Piao HT; Chen S; Wang XC; Jiao XC; Yin XC; Tan KY; Yang YL Perfluoroalkyl Acids in Surface Waters and Tapwater in the Qiantang River Watershed—Influences from Paper, Textile, and Leather Industries. Chemosphere 2017, 185, 610–617. 10.1016/j.chemosphere.2017.06.139. [PubMed: 28719881]

Lu S; Liu Q; Han R; Guo M; Shi J; Song C; Ji N; Lu X; Ma D Potential Applications of Porous Organic Polymers as Adsorbent for the Adsorption of Volatile Organic Compounds. J. Environ. Sci. (China) 2021, 105, 184–203. 10.1016/j.jes.2021.01.007. [PubMed: 34130835]

Lyubimenko R; Gutierrez Cardenas OI; Turshatov A; Richards BS; Schäfer AI Photodegradation of Steroid-Hormone Micropollutants in a Flow-through Membrane Reactor Coated with Pd(II)-Porphyrin. Appl. Catal. B Environ 2021, 291, 120097. 10.1016/j.apcatb.2021.120097.

Ma X; Chai Y; Li P; Wang B Metal-Organic Framework Films and Their Potential Applications in Environmental Pollution Control. Acc. Chem. Res 2019, 52 (5), 1461–1470. 10.1021/acs.accounts.9b00113. [PubMed: 31074608]

Natera J; Massad W; García NA The Role of Vitamin B6 as an Antioxidant in the Presence of Vitamin B2-Photogenerated Reactive Oxygen Species. A Kinetic and Mechanistic Study. Photochem. Photobiol. Sci 2012, 11 (6), 938–945. 10.1039/c2pp05318g. [PubMed: 22231514]

Neves CMB; Filipe OMS; Mota N; Santos SAO; Silvestre AJD; Santos EBH; Neves MGPMS; Simões MMQ Photodegradation of Metoprolol Using a Porphyrin as Photosensitizer under Homogeneous and Heterogeneous Conditions. J. Hazard. Mater 2019, 370, 13–23. 10.1016/j.jhazmat.2018.11.055. [PubMed: 30503313]

Orsuwan A; Kwon S; Bumbudsanpharoke N; Ko S Novel LDPE-Riboflavin Composite Film with Dual Function of Broad-Spectrum Light Barrier and Antimicrobial Activity. Food Control 2019, 100, 176–182. 10.1016/j.foodcont.2019.01.012.

Oulton RL; Kohn T; Cwiertny DM Pharmaceuticals and Personal Care Products in Effluent Matrices: A Survey of Transformation and Removal during Wastewater Treatment and Implications for Wastewater Management. J. Environ. Monit 2010, 12 (11), 1956–1978. 10.1039/c0em00068j. [PubMed: 20938541]

Paczkowski J; Lamberts J; Paczkowska B; Neckers D Photophysical Properties of Rose Bengal and Its Derivatives (XII). Adv. Free Radic. Biol. Med 1985, 1 (5–6), 341–351. 10.1016/8755-9668(85)90075-4.

Quesada HB; Baptista ATA; Cusioli LF; Seibert D; de Oliveira Bezerra C; Bergamasco R Surface Water Pollution by Pharmaceuticals and an Alternative of Removal by Low-Cost Adsorbents: A Review. Chemosphere 2019, 222, 766–780. 10.1016/j.chemosphere.2019.02.009. [PubMed: 30738319]

Rhee HW; So JC; Sang HY; Yong OJ; Hun HP; Pinto RM; Cameselle JC; Sandoval FJ; Roje S; Han K; et al. A Bifunctional Molecule as an Artificial Flavin Mononucleotide Cyclase and a Chemosensor for Selective Fluorescent Detection of Flavins. J. Am. Chem. Soc 2009, 131 (29), 10107–10112. 10.1021/ja9018012. [PubMed: 19569646]

de La Rochette A; Silva E; Birlouez-Aragon I; Mancini M; Edwards A-M; Morlière P Riboflavin Photodegradation and Photosensitizing Effects Are Highly Dependent on Oxygen and Ascorbate Concentrations. Photochem. Photobiol 2000, 72 (6), 815. 10.1562/0031-8655(2000)072<0815:rpapea>2.0.co;2. [PubMed: 11140271]

Routoula E; Patwardhan SV Degradation of Anthraquinone Dyes from Effluents: A Review Focusing on Enzymatic Dye Degradation with Industrial Potential. Environ. Sci. Technol 2020, 54 (2), 647–664. 10.1021/acs.est.9b03737. [PubMed: 31913605]

Saenger W. Cyclodextrin Inclusion Compounds in Research and Industry. Angew. Chemie Int. Ed. English 1980, 19 (5), 344–362. 10.1002/anie.198003441.

Sahoo SK; Das AA; Deka D; Naik B; Kumar Sahoo N Organic-Inorganic Hybrid Hydroquinone Bridged V-CdS/HAP/Pd-TCPP: A Novel Visible Light Active Photocatalyst for Phenol Degradation. J. Mol. Liq 2021, 339, 116721. 10.1016/j.molliq.2021.116721.

Schuman Jorns M; Schöllnhammer G; Hemmerich P Intramolecular Addition of the Riboflavin Side Chain: Anion-Catalyzed Neutral Photochemistry. Eur. J. Biochem 1975, 57 (1), 35–48. 10.1111/j.1432-1033.1975.tb02274.x. [PubMed: 240721]

Sikorska E; Khmelinskii IV; Prukała W; Williams SL; Patel M; Worrall DR; Bourdelande JL; Koput J; Sikorski M Spectroscopy and Photophysics of Lumiflavins and Lumichromes. J. Phys. Chem. A 2004, 108 (9), 1501–1508. 10.1021/jp037048u.

Tang P; El-Moghazy AY; Ji B; Nitin N; Sun G Unique “Posture” of Rose Bengal for Fabricating Personal Protective Equipment with Enhanced Daylight-Induced Biocidal Efficiency. Mater. Adv 2021, 2 (11), 3569–3578. 10.1039/d1ma00100k. [PubMed: 34179787]

Tang P; Ji B; Sun G Wearable Super-Adsorptive Fibrous Equipment: In Situ Grafted with Porous Organic Polymers for Carcinogenic Fumigant Defense and Detoxification. J. Mater. Chem. A 2020, 8 (45), 24128–24136. 10.1039/d0ta07475f.

Tsai WT; Lee MK; Su TY; Chang YM Photodegradation of Bisphenol-A in a Batch TiO2 Suspension Reactor. J. Hazard. Mater 2009, 168 (1), 269–275. 10.1016/j.jhazmat.2009.02.034. [PubMed: 19285792]

Vakili M; Mojiri A; Kindaichi T; Cagnetta G; Yuan J; Wang B; Giwa AS Cross-Linked Chitosan/Zeolite as a Fixed-Bed Column for Organic Micropollutants Removal from Aqueous Solution, Optimization with RSM and Artificial Neural Network. J. Environ. Manage 2019, 250, 109434. 10.1016/j.jenvman.2019.109434. [PubMed: 31472379]

Wang H; Li Z; Yahyaoui S; Hanafy H; Seliem MK; Bonilla-Petriciolet A; Luiz Dotto G; Sellaoui L; Li Q Effective Adsorption of Dyes on an Activated Carbon Prepared from Carboxymethyl Cellulose: Experiments, Characterization and Advanced Modelling. Chem. Eng. J 2021, 417, 128116. 10.1016/j.cej.2020.128116.

Xie H; Jiang W; Liu T; Wu Y; Wang Y; Chen B; Niu D; Liang B Low-Energy Electrochemical Carbon Dioxide Capture Based on a Biological Redox Proton Carrier. Cell Reports Phys. Sci 2020, 1 (5), 100046. 10.1016/j.xcrp.2020.100046.

Xue R; Guo H; Yue L; Wang T; Wang M; Li Q; Liu H; Yang W Preparation and Energy Storage Application of a Long-Life and High Rate Performance Pseudocapacitive COF Material Linked with-NH-Bonds. New J. Chem 2018, 42 (16), 13726–13731. 10.1039/c8nj01942h.

Yi S; Sun S; Fan Y; Zou Y; Dai F; Si Y Scalable Fabrication of Rechargeable Photoactive Cellulose Nanofibrous Membranes for Efficient Degradation of Dyes. Cellulose 2020, 27 (9), 5285–5296. 10.1007/s10570-020-03168-9.

Zhang Z; Si Y; Sun G Photoactivities of Vitamin K Derivatives and Potential Applications as Daylight-Activated Antimicrobial Agents. ACS Sustain. Chem. Eng 2019, 7 (22), 18493–18504. 10.1021/acssuschemeng.9b04449.

Zhang Z; Wisuthiphaet N; Nitin N; Wang L; Kawakita R; Jeoh T; Sun G Photoactive Water-Soluble Vitamin K: A Novel Amphiphilic Photoinduced Antibacterial Agent. ACS Sustain. Chem. Eng 2021, 9 (24), 8280–8294. 10.1021/acssuschemeng.1c02690.

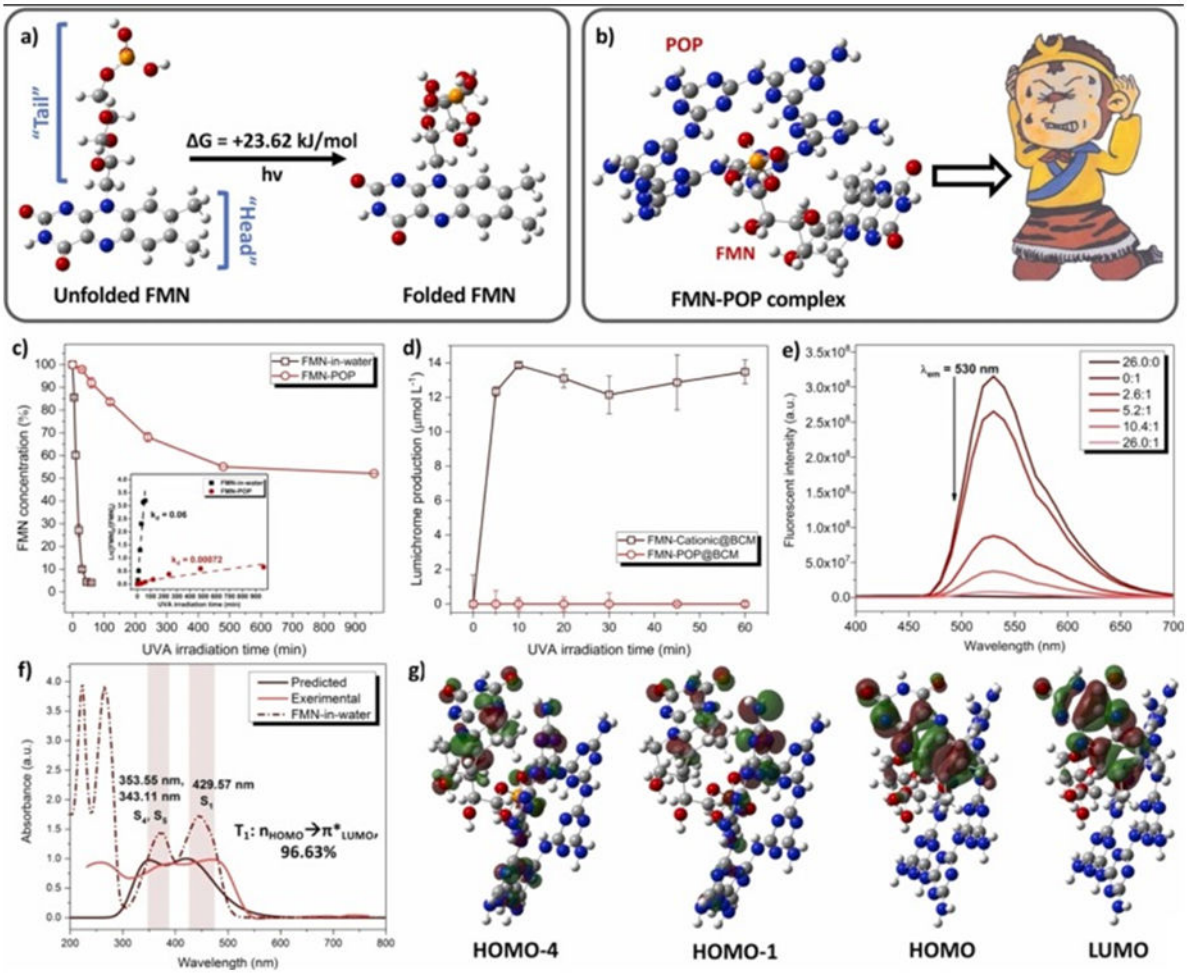

Fig. 1.

a) Unfolded and folded geometry of FMN and the Gibbs free energy difference between two geometries at 298.15 K and 1 atm. b) The optimized geometry of the FMN-POP complex (The Monkey King: picture credit to Miss. Chuhan Luo). c) Time-dependent degradation and kinetics of FMN in solution and in POP. The FMN concentration in the solution (72 mg L−1) was prepared according to the uptake of FMN in POP (i.e., 34.10 mg g−1 measured by ICP-MS) d) Time-dependent production of lumichrome from FMN self-degradation under different POP: FMN ratios. e) Fluorescence spectra of FMN-POP complexes with different POP: FMN molar ratios. f) Predicted and experimental UV–vis spectra, and g) photoexcitation related molecular orbitals of the FMN-POP complex. HOMO and LUMO represent the highest occupied molecular orbital and the lowest unoccupied orbital, respectively.

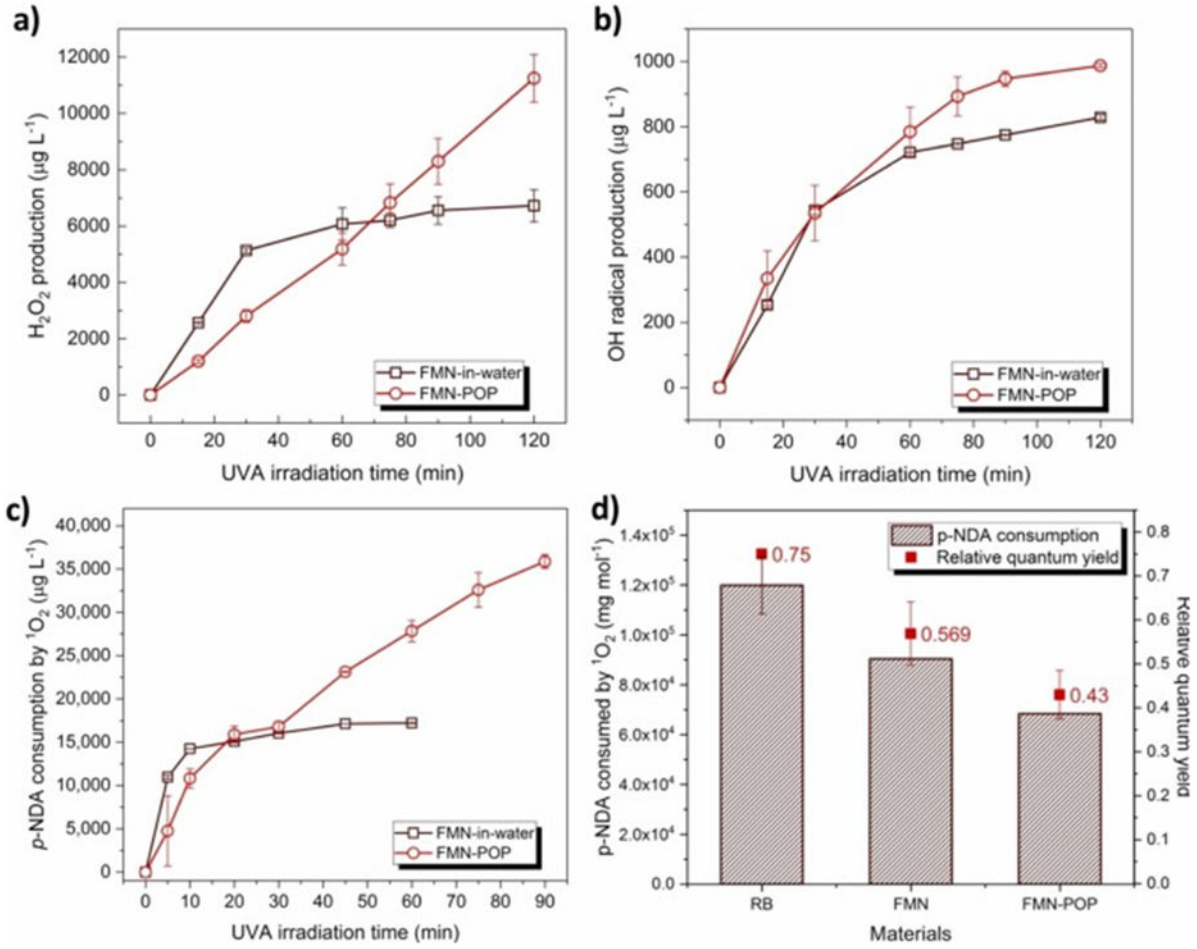

Fig. 2.

Time-dependent UVA-induced production of a) H2O2, b) hydroxyl radical, and c) singlet oxygen by FMN-in-water and FMN-POP particles. d) Relative quantum yields of singlet oxygen of FMN-in-water and FMN-POP particles in H2O by taking rose Bengal as a benchmark.

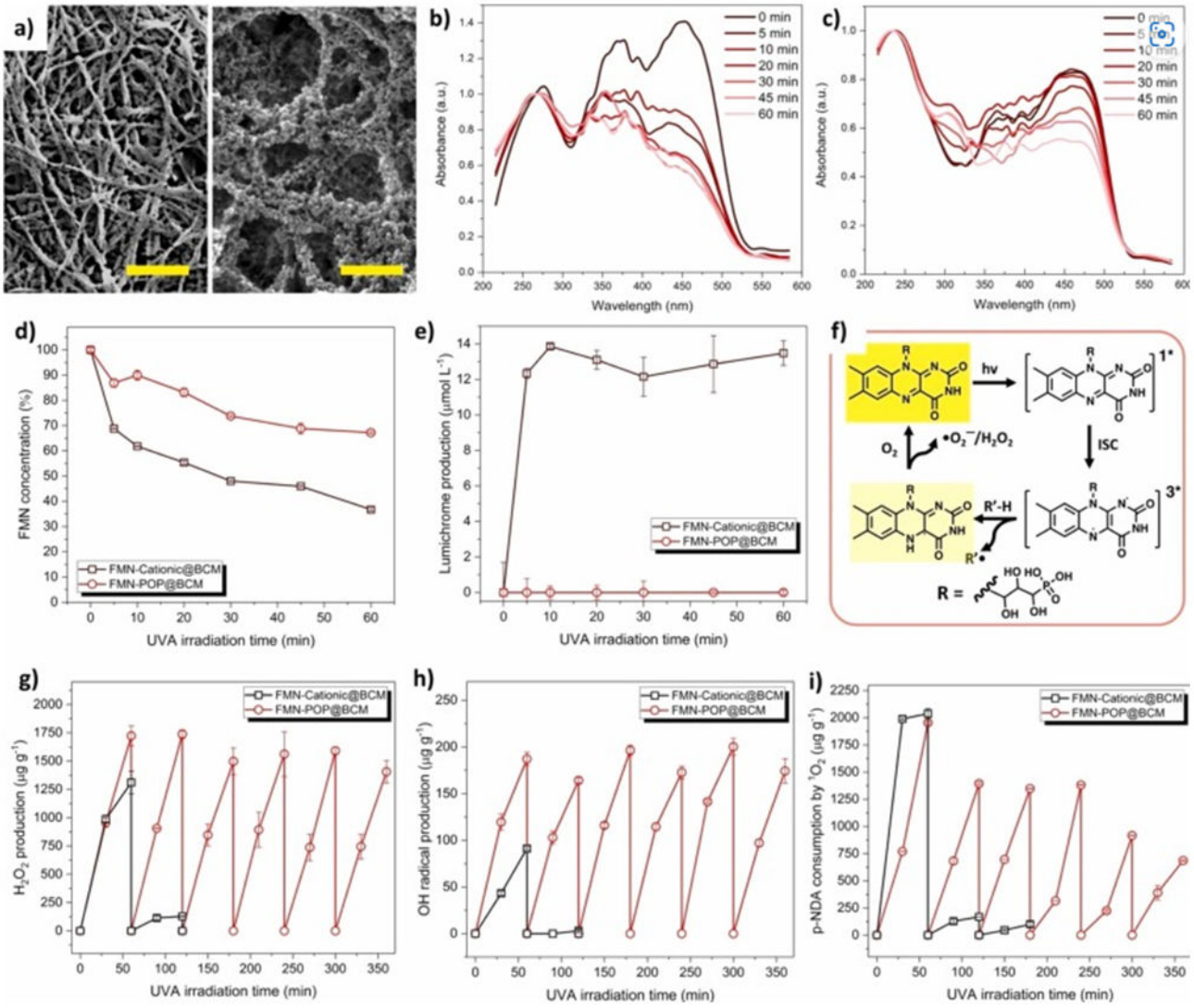

Fig. 3.

a) SEM images of FMN-Cationic@BCM (left) and FMN-POP@BCM (right). The yellow bar refers to 500 nm. DRS of b) FMN-Cationic@BCM and c) FMN-POP@BCM after different UVA irradiation times. d) Self-degradation of FMN and e) production of lumichrome on nanofibrous membranes according to UVA irradiation time. f) Reaction pathway of FMN under light treatment with performing recyclable ROS production. Continuous production of g) H2O2, h) HO•, and i) 1O2 by FMN decorated nanofibrous membranes under UVA irradiations

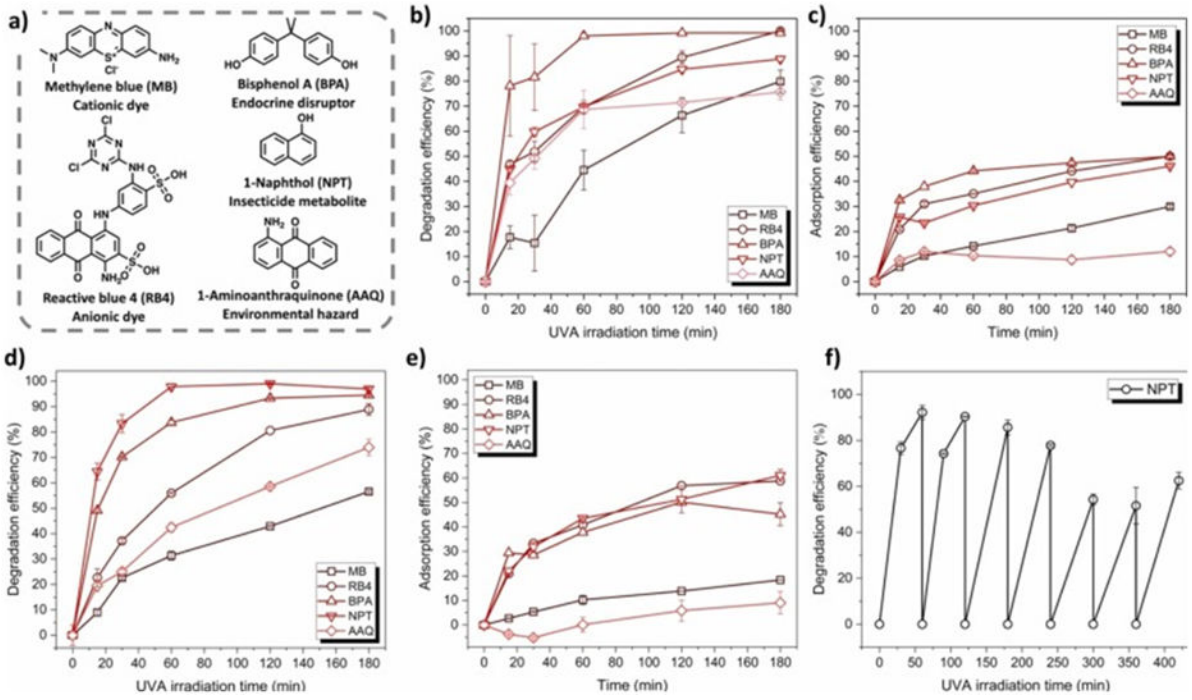

Fig. 4.

Removal of different micropollutants (0.1 mM) in water. a) Chemical structures of interested micropollutants in this study. b) Time-dependent photo-degradation (UVA light) and c) adsorption (under dark) by FMN-POP particles. d) Time-dependent photo-degradation (UVA light) and e) adsorption (under dark) by FMN-POP@BCM. f) Repeated photo-degradation of NPT by FMN-POP@BCM.

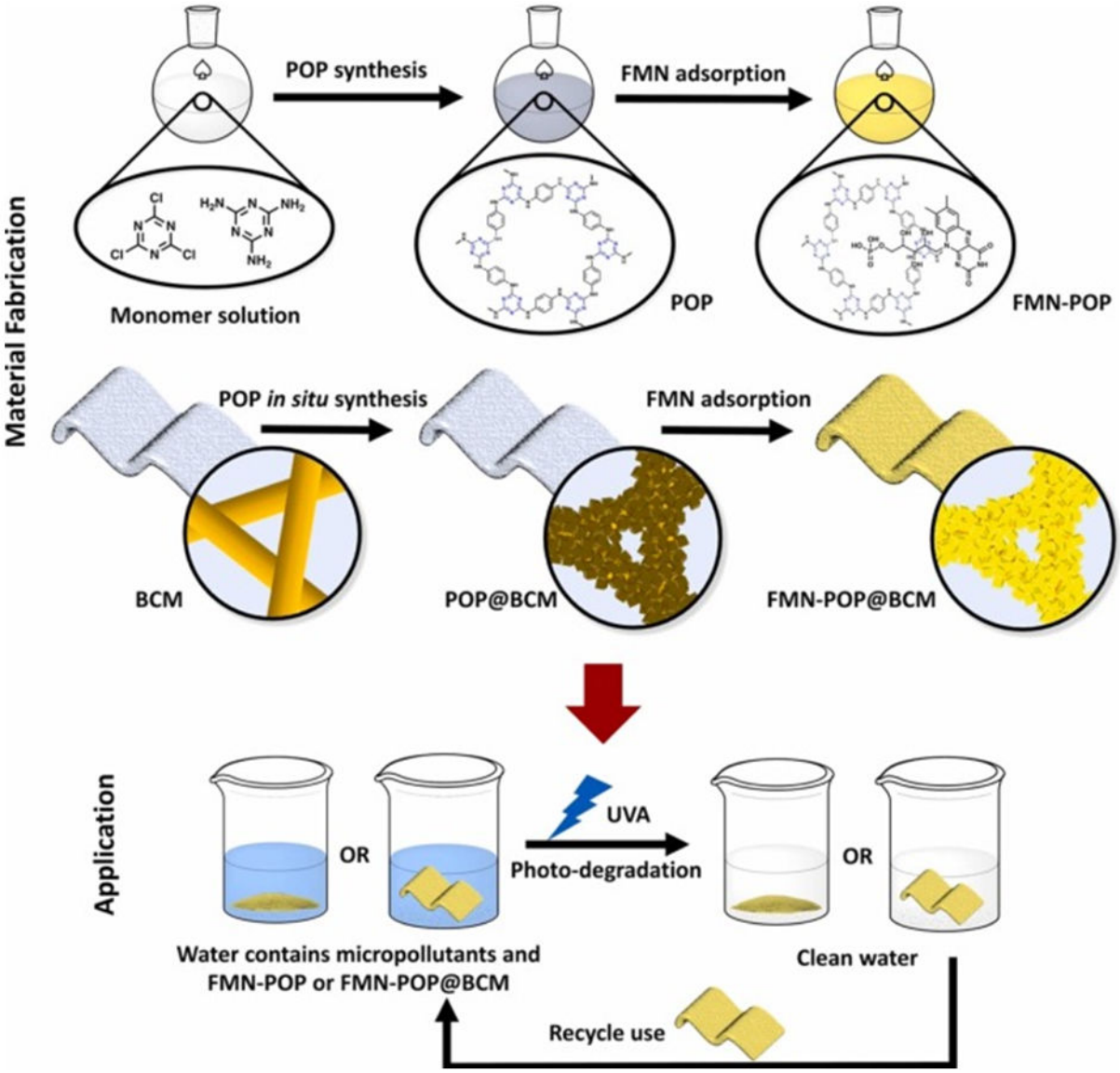

Scheme 1.

Fabrication and application of FMN-POP particles and FMN-POP@BCM on micropollutant photo-degradation.